Spectroscopy and coherence of an excited-state transition in Tm^{3+}:$YAlO_3$ at telecommunication wavelength

Luozhen Li,[1,2,*] Akshay Babu Karyath,[1,2,*] Julien Bertrand,[1,2] Mohsen Falamarzi Askarani,[3,†] Maria Gieysztor,[3,4] Hridya Meppully Sasidharan,[3] Joshua A. Slater,[3,‡] Aaron D. Marsh,[5,§] Philip J. T. Woodburn,[5,‖] Charles W. Thiel,[5] Rufus L. Cone,[5] Sara Marzban,[3,¶] Nir Alfasi,[3,**] Patrick Remy,[6] and Wolfgang Tittel[1,2,††]

[1]*Department of Applied Physics, University of Geneva, 1211 Geneva, Switzerland*
[2]*Constructor University Bremen, 28759 Bremen, Germany*
[3]*QuTech, Delft Technical University, 2628 CJ Delft, Netherlands*
[4]*Institute of Physics, Faculty of Physics, Astronomy and Informatics, Nicolaus Copernicus University, Torun, Poland*
[5]*Department of Physics, Montana State University, Bozeman, Montana 59717-3840, USA*
[6]*SIMH Consulting, Rue de Genève 18, 1225 Chêne-Bourg, Switzerland*

(Received 10 November 2025; accepted 3 August 2026; published 8 September 2026)

We characterize spectroscopic and coherence properties of the 1451.37 nm excited-state zero-phonon line (ZPL) between the $^3F_4$ and the $^3H_4$ manifolds of a thulium-doped yttrium aluminum perovskite (Tm^{3+}:$YAlO_3$) crystal at temperatures around 1.5 K. We measure the absorption spectrum between $^3H_6$ - $^3F_4$ and $^3F_4$ - $^3H_4$ manifolds, the inhomogeneous broadening of the $^3F_4$ - $^3H_4$ (excited-state) ZPL, and the lifetimes of the higher-lying and lower-lying excited states. We also investigate level shifts caused by the quadratic Zeeman interaction as well as spectral hole-burning spectra with varying magnetic fields, providing insights into hyperfine interactions. Using spectral holes again but also optical free induction decays, we assess optical coherence times, finding a maximum of 4.75 ± 0.07 μs at $B = 2$ T and low ion concentration in the $^3F_4$ level. Our results—the first to demonstrate coherence of an excited-state transition in a rare-earth crystal—suggest the possibility of exploiting such transitions for quantum technology.

DOI: 10.1103/73jf-lvyk

I. INTRODUCTION

Starting with the development of protocols that enable the storage and faithful recall of quantum states of light 20 years ago [1–3], trivalent rare-earth ions doped into cryogenically cooled inorganic crystals have played an increasingly important role in the development of quantum technology [4]. Today, ensemble-based quantum memories have reached a level of performance that allows early demonstrations of quantum repeater infrastructure [5–10], and individual ions are being explored as single-photon sources [11,12] and as qubits that allow quantum information processing [13–15]. At the heart of these applications is an important fundamental property—highly coherent transitions between electronic and spin levels with coherence times that can exceed milliseconds [16–19] and hours [20], respectively (see the Supplemental Material [21]).

Surprisingly, while transitions between different (long-lived) excited states play an important role in solid-state lasers, e.g., the Nd-YAG laser [22], optical coherence at cryogenic temperatures of a few Kelvin has so far only been investigated for transitions starting at an electronic ground state. However, the long excited-state lifetimes that characterize the $4f$ levels of rare-earth ions allow, in principle, similarly long coherence times for excited-state transitions. In addition to being of fundamental interest, this would extend the use of rare-earth crystals to new wavelengths and novel applications. Here, we investigate spectroscopic properties and optical coherence of the $^3F_4$ to $^3H_4$ excited-state transition in Tm^{3+}:$YAlO_3$.

Several properties make Tm^{3+}:$YAlO_3$ a particularly interesting material to study. First, the transitions between its $^3F_4$ and the $^3H_4$ electronic manifolds comprise a so-called zero-phonon line (ZPL), i.e., a potentially coherent transition between their lowest Stark levels (or crystal field levels) [see Fig. 1(a) for a simplified level scheme that shows the ZPL between Y1 and X1].

Second, the wavelength of the $^3F_4$ to $^3H_4$ ZPL is around 1450 nm, where transmission loss in standard optical fiber is almost as small as in the telcom C band, 0.25 and 0.2 dB/km, respectively. This makes Tm^{3+}:$YAlO_3$ a potential alternative to erbium-doped crystals, which feature a ground-state

---

*These authors contributed equally to this work.
†Present address: Xanadu Quantum Technologies Inc., Toronto, Ontario M5G 2C8, Canada.
‡Present address: Q*Bird BV, 2628 XJ Delft, Netherlands.
§Present address: Intel Corporation, Hillsboro, Oregon, USA.
‖Present address: S2 Corporation, Bozeman, Montana, USA.
¶Present address: PiCard Systems BV, 6525 EC Nijmegen, Netherlands.
**Present address: Quantum Machines, Tel Aviv, Israel.
††Contact author: wolfgang.tittel@unige.ch

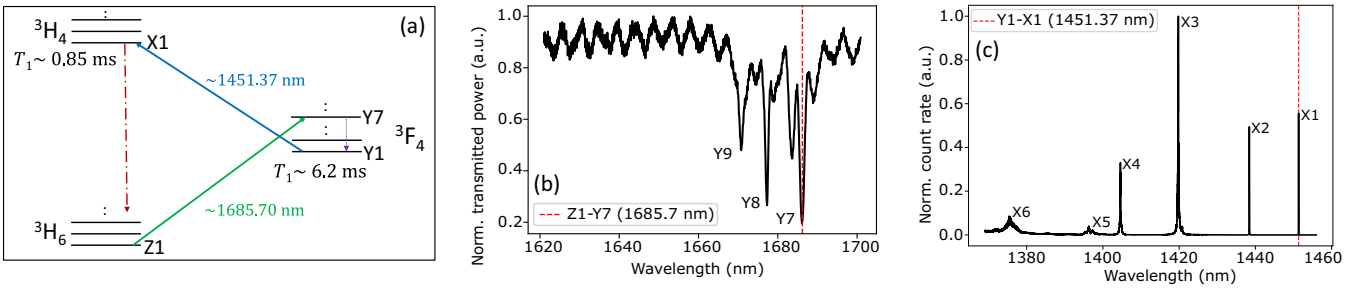

FIG. 1. (a) Energy levels of relevant transitions of Tm^{3+} in $YAlO_3$. (b) Transmission spectrum measured using a broadband LED, showing absorption of the Z1 to $^3F_4$ transitions. (c) Photoluminescence rate at ~800 nm as a function of wavelength of a laser exciting the Y1 to $^3H_4$ transitions. Crystal field levels of the upper manifolds are identified in panels (b) and (c).

transition at around 1532 nm with optical coherence times up to 4.38 ms [17]. Er-doped crystals have been exploited for both single-photon sources and quantum memory for light [23–25].

And third, also shown in Fig. 1(a), Tm^{3+}:$YAlO_3$ features three ZPLs—two ground-state transitions and one excited-state transition—that are arranged in a ring. This may allow the development and implementation of novel protocols that require more than a single line, e.g., the creation of energy-time entangled photon pairs using two cascading transitions [transitions X1-Y1 and Y1-Z1 in Fig. 1(a)] as originally proposed in Ref. [26], and quantum computing using one transition for optical state readout (e.g., transition Z1-X1) and another transition (e.g., transition Z1-Y1) for dipole-blockade-based controlled two-qubit gates, similar to the case of trapped ions [27].

The energy-level structure of Tm^{3+}:$YAlO_3$ has been characterized before [28–31]. However, to the best of our knowledge, our investigation is the first to study the excited-state transition of Tm^{3+}:$YAlO_3$—more precisely of any rare-earth crystal—at cryogenic temperatures where coherence properties can be assessed.

Our paper is organized as follows. First, we measure the absorption spectrum between the $^3H_6$ and $^3F_4$ manifolds, and we describe how we populate the Y1 level. We then extend the absorption measurements to transitions between the $^3F_4$ and $^3H_4$ manifolds, and we characterize the inhomogeneous broadening of the ZPL at 1451.37 nm as well as the lifetimes of the Y1 and X1 levels. Moving on to magnetic interactions, we study the quadratic Zeeman shift affecting the ~1451.3 nm transition, and we study level splittings by means of spectral hole burning. We also assess optical coherence as a function of magnetic field, wait time between excitation and readout, and ion concentration in the Y1 level using again spectral holes as well as free induction decays (FIDs). To round off the paper, we discuss next steps toward applications of Tm^{3+}:$YAlO_3$ in quantum information processing. Details of the crystal, the experimental setup, and the quadratic Zeeman shift measurements are provided in the Appendixes.

II. MEASUREMENTS

A. Optical pumping

At 1.5 K, the Tm^{3+} ions occupy the lowest crystal field level Z1. Since we are interested in the Y1 to X1 transition, our first goal is to populate the Y1 level. Toward this end, we can pump ions into any crystal field level within the $^3F_4$ manifold. Since intramanifold relaxation between different levels takes place on the nanosecond timescale [32], all ions in levels Y2 to Y9 will rapidly decay into Y1. This approach to pumping is promising since it allows one to interact continuously with an empty upper atomic level. In addition, one can choose the strongest absorption line. An alternative possibility is described in the Supplemental Material [21].

B. Absorption spectra

We study the absorption lines between Z1 and the $^3F_4$ manifold by measuring the wavelength-dependent transmission of the broadband SLED using an optical spectrum analyzer (Anritsu MS9710C) [see Fig. 1(b)] (see Ref. [28] for the association of absorption lines with energy levels). After optimization of polarization using a fiber-optic polarization controller, we find that the Z1 to Y7 transition at 1685.7 nm features the strongest absorption. It is used in the following to populate the Y1 level.

Next, we measure the absorption spectrum of the Y1 to $^3H_4$ transitions, still at $B = 0$ T. After populating Y1 using the 1686 nm laser, we expose the crystal to laser light whose wavelength we scan between 1370 and 1456 nm in steps of 0.01 nm. The detection of photoluminescence (PL) around 800 nm indicates resonances and, at the same time, allows optimizing the laser polarization and the initial pumping step. Our measurement results are shown in Fig. 1(c). In particular, we find a well-isolated line at 1451.37 nm—the ZPL between Y1 and X1 [29]. A subsequent laser scan around this wavelength with improved resolution of 0.001 nm reveals a linewidth of 1.29 GHz. This is much narrower than any of the nanometer-wide ground-state transitions shown in Fig. 1(b). We furthermore measure an optical depth of up to 1.12 on line center, which we expect to increase with optimized pumping (see the Supplemental Material [21]).

Small measurement variations allow establishing the radiative lifetimes of the Y1 and the X1 levels. For the former, we monitor the time-resolved decay of the optical depth of the Y1 to X1 transition after switching off the 1686 nm laser. For the latter, we analyze the decay of the 800 nm PL rate after pulsed excitation of the X1 level. We find lifetimes of 6.21 ± 0.01 ms and 845.4 ± 2.4 μs for the $^3F_4$ and the $^3H_4$ levels, respectively, which is consistent with literature values

[33] and an alternative approach detailed in the Supplemental Material [21].

C. Level shifts and splitting

The magnetic field-dependent change of the Tm energy levels is described by the Hamiltonian

$$H = \mathbf{B} \cdot (-g_n \beta_n \mathbb{1} - 2g\mu_B A\, \mathbf{\Lambda}) \cdot \mathbf{I} - g^2 \mu_B^2 \mathbf{B} \cdot \mathbf{\Lambda} \cdot \mathbf{B}, \quad (1)$$

where the first part describes level splitting due to the enhanced nuclear Zeeman effect (the combination of the nuclear Zeeman interaction and the second-order coupling between the hyperfine interaction and the electronic Zeeman effect) and the last part describes level shifts caused by the quadratic Zeeman interaction. Here, g_n is the nuclear g factor of Tm, β_n the nuclear magneton, g the Landé g factor for each level, μ_B the Bohr magneton, A the hyperfine constant, $\mathbf{I}$ the ion's nuclear spin, $\mathbf{B}$ the applied magnetic field, and Λ the hyperfine tensor [34].

First, to quantify the quadratic Zeeman effect, we measure the shift of the Y1 to X1 transition as a function of applied magnetic field, yielding $\Delta\nu = -101 \pm 3$ MHz/T^2 (see Appendix B).

Second, to assess the magnetic field-dependent energy-level splitting of the thulium ions as a consequence of the enhanced nuclear Zeeman effect, we perform a series of spectral hole burning experiments. After populating Y1, we expose the Tm ions during a *burn time* of 300 μs to narrow-bandwidth 1451 nm laser light. After 10 μs, we start scanning the 1451 nm laser over a 200 MHz wide spectral interval that is centered on the burn frequency and we monitor the transmitted optical power. We define the *wait time* as the time between the end of the burn pulse and the moment when the scanning laser features the same frequency as the burn pulse, i.e., the moment when it scans over the previously created spectral hole, here 85 μs. For these measurements, we kept the density of the ions in the $^3F_4$ level constant and we burned the spectral hole at the center of the Y1 ↔ X1 (1451 nm) line—the optical depth was around 0.4. Figure 2 shows the resulting hole-burning spectra for magnetic fields between 0 and 2 T, consisting of a central hole and two clusters of side holes on either side. We find that the width of the central hole decreases with increasing magnetic field and that the center of each cluster of side holes shifts linearly at rates of ±25.6 and ±41.6 MHz/T away from the center. The two holes within each cluster also split as a function of the field at a rate of 2–3 MHz/T. We attribute this substructure within each cluster to a slight misalignment of the magnetic field with respect to the crystal b axis, in which case the two pairs of Tm sites feature different level splittings (see Appendix A). We also note the absence of antiholes, i.e., narrow spectral regions with increased absorption.

To explain the origin of the clusters, we take into account that Tm has a nuclear spin $I = 1/2$, and that the hyperfine coupling between the nuclear spin and the electronic states splits each crystal field level into a pair of hyperfine levels [35]. As we further illustrate in the Supplemental Material [21], narrow-bandwidth optical pumping therefore drives four different transitions within the ensemble of inhomogeneously broadened thulium ions—one between each combination of

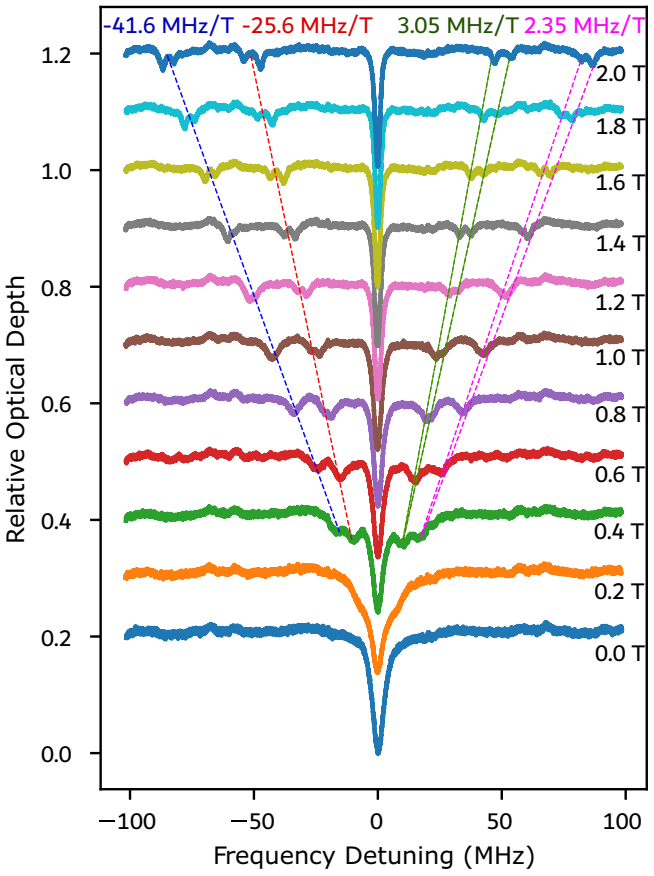

FIG. 2. Spectral hole burning spectra under varying magnetic fields. Traces measured with different fields are offset by an amount that is proportional to the field, and splitting rates are indicated.

a ground state and an excited state. This results in decreased absorption—a central hole and four side holes—at five different frequencies. Note that the sum of the burn and wait time is sufficiently small compared to the lifetime of the two magnetic X1 levels to exclude significant decay of atoms from X1 back into Y1 (in addition, the branching ratio for this pathway is rather small, and most decay leads back to the ground state). This explains the absence of antiholes.

Next, we perform time-resolved spectral hole burning. We find that the two "inner" clusters (with splitting rate of ±25.6 MHz/T) decay on a scale comparable to the radiative lifetime of X1 (0.85 ms). As explained in the Supplemental Material [21], this suggests that these clusters are caused by the splitting of the two hyperfine levels within the Y1 doublet. The other pairs of clusters, with splitting rate of ±41.6 MHz/T, decay with a much longer lifetime, comparable to that of the central hole. We conjecture that they are caused by the splitting of the two hyperfine levels within the X1 doublet.

D. Optical coherence

In addition to providing insight into hyperfine interactions, the hole-burning spectra—more precisely the width of the central holes—also allow one to derive an upper bound for the homogeneous linewidth γ_{hom} and hence a lower bound for the optical coherence time $T_2 = 1/(\pi\gamma_{\mathrm{hom}})$ of the

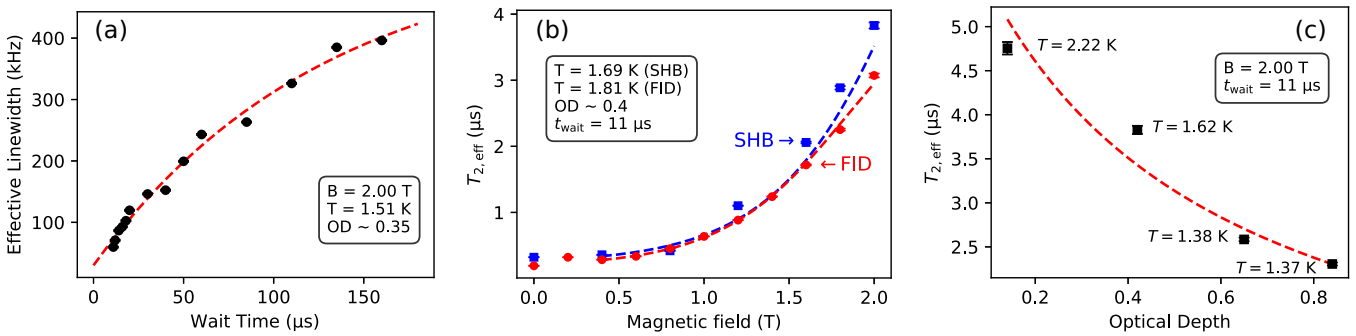

FIG. 3. (a) Effective linewidths measured using spectral holes with varying wait time and $B = 2$ T. The red dashed line is a fit based on Eq. (2). (b) Effective optical coherence times for different magnetic fields obtained by means of spectral hole burning (blue squares, $t_{\mathrm{wait}} = 11$ μs) and free induction decay (red circles). The dashed lines are fits based on a spectral diffusion model [36]. (c) Effective optical coherence times measured using spectral hole buring (SHB) as a function of optical depth. The temperature varied significantly between measurements. The dashed line is a fit based on a model considering instantaneous spectral diffusion [37]. All data points in panels (a)–(c) are corrected with respect to the laser linewidth of 170 kHz, and error bars are based on an uncertainty of that linewidth of ±2 kHz.

excited-state transition. Indeed, one can show that $\gamma_{\mathrm{hole}} = \gamma_{\mathrm{hom}}(1 + \sqrt{1 + \chi^2 T_1 T_2}) + \gamma_{\mathrm{laser}}$ [38], where γ_{hole} is the full width at half maximum of the hole, χ is the on-resonance Rabi frequency, and T_1 is the radiative lifetime. Furthermore, γ_{laser} describes the linewidth of the laser used for hole burning, which we measured by delay self-homodyne interferometric detection [39] to be 171.1 ± 2.0 kHz. When the power of the burn pulse is sufficiently small (and $\chi^2 \approx 0$), this equation can be simplified to $\gamma_{\mathrm{hole}} \approx 2\gamma_{\mathrm{hom}} + \gamma_{\mathrm{laser}}$.

First, to characterize the effect of spectral diffusion, we analyze the evolution of the measured (effective) homogeneous linewidth as a function of wait time t_{wait}. Following Ref. [36], it can be described as

$$\gamma_{\mathrm{eff}} = (\gamma_{\mathrm{hole}} - \gamma_{\mathrm{laser}})/2 = \gamma_0 + \frac{\gamma_{\mathrm{SD}}}{2}[1 - e^{-R t_{\mathrm{wait}}}], \quad (2)$$

where γ_0 is the intrinsic linewidth (no spectral diffusion), and γ_{SD} and R describe the maximum broadening due to spectral diffusion and the rate with which the maximum is reached, respectively. The latter equals the average spin-flip rate of the spin bath around the probed ions.

Figure 3(a) shows γ_{eff} as a function of t_{wait}, varied between 11 and 161 μs at $B = 2$ T. The data are well described by Eq. (2) and show the presence of significant spectral diffusion on the timescale of our measurements. The fit gives an average bath spin-flip rate $R = 7.82 \pm 1.75$ kHz, which corresponds to a characteristic spectral diffusion timescale of $1/R \approx 128$ μs, and a maximum linewidth $\gamma_{\mathrm{eff}}^{\mathrm{max}} = 550.9 \pm 60.3$ kHz (for $\gamma_0 = 30.0 \pm 9.7$ kHz and $\gamma_{\mathrm{SD}} = 1041.7 \pm 119.1$ kHz).

Figure 3(b) depicts $T_{2,\mathrm{eff}}$ for a fixed wait time of $t_{\mathrm{wait}} = 11$ μs and different magnetic fields, where $T_{2,\mathrm{eff}} = 1/(\pi\gamma_{\mathrm{eff}})$ is the effective optical coherence time. Another way to assess the optical coherence time is via the FID [40]. In this case, ions are excited using a pulsed laser (pulse duration of 20 μs) with a bandwidth that is smaller than the homogeneous linewidth of the transition to be studied. The thereby created atomic polarization gives rise to the emission of light, which decreases exponentially after the end of the laser pulse due to atomic dephasing.

As shown in the Supplemental Material [21], $\tau_{\mathrm{FID}} = 1/[2\pi(2\gamma_{\mathrm{eff}} + \gamma_{\mathrm{laser}})]$, where τ_{FID} is the $1/e$ decay of the intensity of the FID signal. After solving for γ_{eff}, this leads to

$$T_{2,\mathrm{eff}} = \frac{4}{1/\tau_{\mathrm{FID}} - 2\pi\gamma_{\mathrm{laser}}}. \quad (3)$$

Figure 3(b) depicts $T_{2,\mathrm{eff}}$ as a function of magnetic field, along with the results obtained using SHB, as described above. We note the good match between the two datasets. The figure also shows fits of a spectral diffusion model that considers magnetic noise from nearby spin flip-flops and phonon-driven spin flips [36] to both sets. We find that the effect of spin flips can be ignored in the assessed parameter regime. See the Supplemental Material [21] for more information.

Further studies are required to identify the source of spin flip-flops. The nuclear spins of neighboring lattice ions (most likely Al^{3+} [41,42]) are possible contributors, even though their impact seems too small to explain our observations. However, note that the energy difference between the Z1 and Z2 levels in the $^3H_6$ manifold of Tm^{3+} is very small (∼90 GHz). These levels may therefore form non-Kramers quasidoublets that exhibit a strong magnetic moment, the so-called Van Vleck paramagnetism [43,44], which may also contribute to magnetic noise. See the Supplemental Material [21] for more details.

Finally, we vary the ion density in Y1 by changing the optical power during pumping. Since we continue burning spectral holes on line center of the 1451 nm transition, we can parametrize this change in terms of the optical depth of the Y1 ↔ X1 transition. As shown in Fig. 3(b) for $B = 2$ T and $t_{\mathrm{wait}} = 11$ μs, $T_{2,\mathrm{eff}}$ increases to 4.75 ± 0.07 μs as the optical depth is reduced from 0.84 to 0.14. We attribute this dependence to flip-flops between spins of neighboring Tm ions in the Y1 level, or, more likely, to instantaneous spectral diffusion [37] caused by exciting Tm ions to the X1 level. Note that the temperature varied significantly during these measurements. However, since we observed an increase of coherence time with increasing temperature and not the opposite, these variations do not allow explaining our results.

III. CONCLUSION

We have investigated an excited-state transition in Tm^{3+}:$YAlO_3$ at cryogenic temperatures and varying magnetic fields. We observed a quadratic Zeeman shift of the transition wavelength as well as level splittings caused by the enhanced nuclear Zeeman interaction. In addition, we measured for the first time coherence of such a transition in any rare-earth ion-doped crystal. While our findings clearly show that optical coherence of the excited-state transition will continue to increase as the magnetic field is increased beyond 2 T, and t_{wait} and the optical depth are further decreased, more measurements are needed to better understand and mitigate the origin of significant spectral diffusion. Several avenues can be pursued. First, spin flips and flip-flops are suppressed at lower temperature and a longer optical coherence time can thus be expected by further cooling the crystal. For instance, the spectral diffusion model used to fit the data in Fig. 3(b) predicts $T_2 = 10.6$ μs for $T < 0.8$ K, $B = 2$ T, OD $= 0.4$, and $t_{\text{wait}} = 11$ μs (see the Supplemental Material [21]). Second, reducing either the Tm doping concentration, the concentration of Tm ions in the Y1 level, and/or the optical power used to burn spectral holes is expected to lead to a further increase of T_2, with values of several tens of microseconds appearing realistic to reach. Third, the magnetic field can be increased up to a point where spin flips become the primary limitation. This should also reduce the impact of the Van Vleck paramagnetism as the energy gap between the lowest Stark levels in the $^3H_6$ manifold will increase and flip-flops of pseudospins therefore become less likely. And fourth, changing both the magnitude and the direction of the magnetic field may lead to spectrally stable optical clock transitions, which have been reported before for several rare-earth crystals [45,46], including for a Tm-doped crystal [34]. Our finding of a quadratic Zeeman shift is an important first step toward this end.

Overall, our results demonstrate that excited-state transitions in rare-earth ion-doped crystal may be useful for applications in quantum information processing. In particular, the 1450 nm line in Tm may enable the creation of true single-photon sources and quantum memory within a telecom band—a potential alternative to erbium and possibly enabling the creation of quantum networks coexisting with classical communication at 1550 nm over the same fiber infrastructure [47].

ACKNOWLEDGMENTS

The authors thank Javier Carrasco Ávila, Archi Gupta, and Deeksha Gupta for discussions. W.T. acknowledges funding through the Netherlands Organization for Scientific Research under Project No. 601.QT.001-1, the European Union's Horizon 2020 Research and Innovation Program under Grant Agreement No. 820445 and Project Name Quantum Internet Alliance, and the Swiss State Secretariat for Education, Research and Innovation (SERI) under Contract No. UeM019-3. Work at MSU was supported in part by the Air Force Research Laboratory under Award No. FA8750-23-2-0500.

DATA AVAILABILITY

The data that support the findings of this article are openly available [48].

APPENDIX A: EXPERIMENTAL DETAILS

$YAlO_3$ features an orthorombic unit cell with lattice constants $a = 5.179$ Å, $b = 5.329$ Å, and $c = 7.370$ Å (*Pbnm* space group). Tm^{3+} substitutes Y^{3+} ions in four structurally inequivalent positions with low point-group symmetry C_{1h} [29]. Doped Tm^{3+} ions are related pairwise by inversion symmetry, resulting in two pairs of sites that become magnetically equivalent for magnetic fields directed within the *ac* and *bc* planes [49], where *a*, *b*, and *c* denote the principal crystal axes.

Measurements are carried out using $a = 12.0$ mm $\times b = 2.2$ mm $\times c = 2.0$ mm large 0.1% crystal (from Scientific Material Corp.). The crystal is glued to a customized Cu stage and further secured and thermalized by a Cu lid with spring-tensioned screws. It is cooled to around 1.5 K using a pulse-tube cooler supplemented by an adiabatic demagnetization stage. A superconducting solenoid allows one to apply a homogeneous magnetic field between 0 and 2 T approximately along the *b* axis of the crystal.

The laser light is sent through the crystal along the *a* axis using a single-mode pigtailed ferrule and a gradient-index (GRIN) lens. The ferrule is attached to an attocube nanopositioner, which allows adjusting the distance between the ferrule and the GRIN lens to collimate the laser beam to a diameter of around 0.3 mm. Behind the crystal, a mirror reflects the light back through the crystal and into the fiber. A tunable continuous-wave (CW) laser (Toptica DL pro) or an SLED (Denselight Semiconductors DL-BZ1) emitting at around 1680 nm wavelength is used for optical pumping, and another CW laser (Santec TSL-550) drives the excited-state transition at around 1450 nm wavelength. One fiber-based acousto-optic modulator (AOM) per laser allows creating short pulses, and a phase modulator is used to modify the spectrum of the ∼1450 nm laser light.

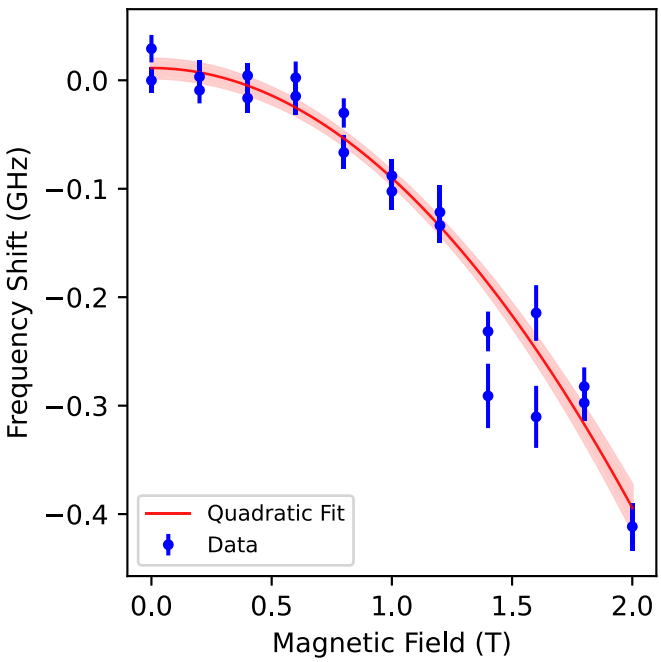

FIG. 4. Frequency shift of the inhomogeneously broadened Y1-X1 transition as a function of magnetic field.

Depending on the experiment, we can choose between different detectors. To detect photoluminescence at 795 nm wavelength caused by atomic decay from the $^3H_4$ to the $^3H_6$ manifold, a single-photon counting module based on a silicon-avalanche photodiode is used (from Perkin Elmer). In this case, we also employ free-space spectral filters (a low-pass filter composed of multiple EO2-coated mirrors and a DMSP950 dichroic mirror, all from Thorlabs) that reject light at 1680 and 1450 nm. For spectral hole burning measurements, the 1450 nm laser light is directed to an InGaAs photoreceiver with 10 MHz bandwidth (New Focus 2053). Finally, to characterize FIDs, a higher-bandwidth photoreceiver (New Focus 1811) with a rise and fall time of 3 ns is used. It is preceded by a gating AOM that blocks irrelevant pulses. For a schematic of the optical setup, see the Supplemental Material [21].

APPENDIX B: QUADRATIC ZEEMAN SHIFT

As described in Eq. (1), the magnetic field-dependent spin Hamiltonian of Tm energy levels contains a term that describes the level shifts caused by the quadratic Zeeman interaction.

Figure 4 shows the frequency shift of the inhomogeneous broadened Y1-X1 transition as a function of magnetic field. For each data point, we measured the frequency at the center of the line. The data are well fitted by a quadratic function $\Delta f = a \times B^2 + c$, yielding $a = -101 \pm 3$ MHz/T^2, and $c = 11 \pm 4$ MHz. The shaded region indicates the 95% confidence interval of the fit. This measurement confirms the quadratic Zeeman interaction described in the spin Hamiltonian.

[1] B. Kraus, W. Tittel, N. Gisin, M. Nilsson, S. Kröll, and J. I. Cirac, Quantum memory for nonstationary light fields based on controlled reversible inhomogeneous broadening, Phys. Rev. A **73**, 020302(R) (2006).

[2] A. L. Alexander, J. J. Longdell, M. J. Sellars, and N. B. Manson, Photon echoes produced by switching electric fields, Phys. Rev. Lett. **96**, 043602 (2006).

[3] M. Nilsson and S. Kröll, Solid state quantum memory using complete absorption and re-emission of photons by tailored and externally controlled inhomogeneous absorption profiles, Opt. Commun. **247**, 393 (2005).

[4] W. Tittel, M. Afzelius, A. Kinos, L. Rippe, and A. Walther, Quantum networks using rare-earth ions, Quantum Sci. Technol. **10**, 033002 (2025).

[5] N. Sangouard, C. Simon, H. De Riedmatten, and N. Gisin, Quantum repeaters based on atomic ensembles and linear optics, Rev. Mod. Phys. **83**, 33 (2011).

[6] N. Sinclair, E. Saglamyurek, H. Mallahzadeh, J. A. Slater, M. George, R. Ricken, M. P. Hedges, D. Oblak, C. Simon, W. Sohler, and W. Tittel, Spectral multiplexing for scalable quantum photonics using an atomic frequency comb quantum memory and feed-forward control, Phys. Rev. Lett. **113**, 053603 (2014).

[7] X. Liu, J. Hu, Z.-F. Li, X. Li, P.-Y. Li, P.-J. Liang, Z.-Q. Zhou, C.-F. Li, and G.-C. Guo, Heralded entanglement distribution between two absorptive quantum memories, Nature (London) **594**, 41 (2021).

[8] D. Lago-Rivera, S. Grandi, J. Rakonjac, A. Seri, and H. de Riedmatten, Telecom-heralded entanglement between multimode solid-state quantum memories, Nature (London) **594**, 37 (2021).

[9] A. Ortu, A. Holzäpfel, J. Etesse, and M. Afzelius, Storage of photonic time-bin qubits for up to 20 ms in a rare-earth doped crystal, npj Quantum Inf. **8**, 29 (2022).

[10] T.-X. Zhu, C. Zhang, Z.-W. Ou, X. Liu, P.-J. Liang, X.-M. Hu, Y.-F. Huang, Z.-Q. Zhou, C.-F. Li, and G.-C. Guo, A metropolitan-scale multiplexed quantum repeater with Bell non-locality, Nat. Photonics **20**, 812 (2026).

[11] A. M. Dibos, M. Raha, C. M. Phenicie, and J. D. Thompson, Atomic source of single photons in the telecom band, Phys. Rev. Lett. **120**, 243601 (2018).

[12] T. Zhong, J. M. Kindem, J. G. Bartholomew, J. Rochman, I. Craiciu, V. Verma, S. W. Nam, F. Marsili, M. D. Shaw, A. D. Beyer, and A. Faraon, Optically addressing single rare-earth ions in a nanophotonic cavity, Phys. Rev. Lett. **121**, 183603 (2018).

[13] M. Raha, S. Chen, C. M. Phenicie, S. Ourari, A. M. Dibos, and J. D. Thompson, Optical quantum nondemolition measurement of a single rare earth ion qubit, Nat. Commun. **11**, 1605 (2020).

[14] J. M. Kindem, A. Ruskuc, J. G. Bartholomew, J. Rochman, Y. Q. Huan, and A. Faraon, Coherent control and single-shot readout of a rare-earth ion embedded in a nanophotonic cavity, Nature (London) **580**, 201 (2020).

[15] A. Gritsch, A. Ulanowski, J. Pforr, and A. Reiserer, Optical single-shot readout of spin qubits in silicon, Nat. Commun. **16**, 64 (2025).

[16] R. W. Equall, Y. Sun, R. L. Cone, and R. M. MacFarlane, Ultraslow optical dephasing in Eu^{3+}:Y_2SiO_5, Phys. Rev. Lett. **72**, 2179 (1994).

[17] T. Böttger, C. W. Thiel, R. L. Cone, and Y. Sun, Effects of magnetic field orientation on optical decoherence in Er^{3+}:Y_2SiO_5, Phys. Rev. B **79**, 115104 (2009).

[18] S. Welinski, A. Tiranov, M. Businger, A. Ferrier, M. Afzelius, and P. Goldner, Coherence time extension by large-scale optical spin polarization in a rare-earth doped crystal, Phys. Rev. X **10**, 031060 (2020).

[19] M. F. Askarani, A. Das, J. H. Davidson, G. C. Amaral, N. Sinclair, J. A. Slater, S. Marzban, C. W. Thiel, R. L. Cone, D. Oblak, *et al.*, Long-lived solid-state optical memory for high-rate quantum repeaters, Phys. Rev. Lett. **127**, 220502 (2021).

[20] M. Zhong, M. P. Hedges, R. L. Ahlefeldt, J. G. Bartholomew, S. E. Beavan, S. M. Wittig, J. J. Longdell, and M. J. Sellars, Optically addressable nuclear spins in a solid with a six-hour coherence time, Nature (London) **517**, 177 (2015).

[21] See Supplemental Material at http://link.aps.org/supplemental/10.1103/73jf-lvyk for additional experimental details, data analysis, and theoretical derivations, which includes Refs. [50–68].

[22] J. Geusic, H. Marcos, and L. Van Uitert, Laser oscillations in Nd-doped yttrium aluminum, yttrium gallium and gadolinium garnets, Appl. Phys. Lett. **4**, 182 (1964).

[23] Y. Yu, D. Oser, G. Da Prato, E. Urbinati, J. C. Ávila, Y. Zhang, P. Remy, S. Marzban, S. Gröblacher, and W. Tittel, Frequency tunable, cavity-enhanced single erbium quantum emitter in the telecom band, Phys. Rev. Lett. **131**, 170801 (2023).

[24] E. Saglamyurek, N. Sinclair, J. Jin, J. A. Slater, D. Oblak, F. Bussieres, M. George, R. Ricken, W. Sohler, and W. Tittel, Broadband waveguide quantum memory for entangled photons, Nature (London) **469**, 512 (2011).

[25] E. Miyazono, T. Zhong, I. Craiciu, J. M. Kindem, and A. Faraon, Coupling of erbium dopants to yttrium orthosilicate photonic crystal cavities for on-chip optical quantum memories, Appl. Phys. Lett. **108**, 011111 (2016).

[26] J. D. Franson, Bell inequality for position and time, Phys. Rev. Lett. **62**, 2205 (1989).

[27] A. H. Myerson, D. J. Szwer, S. C. Webster, D. T. C. Allcock, M. J. Curtis, G. Imreh, J. A. Sherman, D. N. Stacey, A. M. Steane, and D. M. Lucas, High-fidelity readout of trapped-ion qubits, Phys. Rev. Lett. **100**, 200502 (2008).

[28] V. Antonov, P. Arsenev, K. Bienert, and A. Potemkin, Spectral properties of rare-earth ions in $YAlO_3$ crystals, Phys. Stat. Sol. (a) **19**, 289 (1973).

[29] J. M. O'Hare and V. Donlan, Crystal-field determination for trivalent thulium in yttrium orthoaluminate, Phys. Rev. B **14**, 3732 (1976).

[30] J. Körner, T. Lühder, J. Reiter, I. Uschmann, H. Marschner, V. Jambunathan, A. Lucianetti, T. Mocek, J. Hein, and M. C. Kaluza, Spectroscopic investigations of thulium doped YAG and YAP crystals between 77 K and 300 K for short-wavelength infrared lasers, J. Lumin. **202**, 427 (2018).

[31] L. Guillemot, P. Loiko, J.-L. Doualan, A. Braud, and P. Camy, Excited-state absorption in thulium-doped materials in the near-infrared, Opt. Express **30**, 31669 (2022).

[32] C. W. Thiel, T. Böttger, and R. Cone, Rare-earth-doped materials for applications in quantum information storage and signal processing, J. Lumin. **131**, 353 (2011).

[33] L. Guillemot, P. Loiko, A. Braud, J.-L. Doualan, A. Hideur, M. Koselja, R. Moncorge, and P. Camy, Continuous-wave Tm:$YAlO_3$ laser at ∼2.3 μm, Opt. Lett. **44**, 5077 (2019).

[34] J. H. Davidson, P. J. T. Woodburn, A. D. Marsh, K. J. Olson, A. Olivera, A. Das, M. Falamarzi Askarani, W. Tittel, R. L. Cone, and C. W. Thiel, Measurement of the thulium ion spin Hamiltonian in an yttrium gallium garnet host crystal, Phys. Rev. B **104**, 134103 (2021).

[35] N. Sinclair, D. Oblak, E. Saglamyurek, R. L. Cone, C. W. Thiel, and W. Tittel, Optical coherence and energy-level properties of a Tm^{3+}-doped $LiNbO_3$ waveguide at subkelvin temperatures, Phys. Rev. B **103**, 134105 (2021).

[36] T. Böttger, C. W. Thiel, Y. Sun, and R. L. Cone, Optical decoherence and spectral diffusion at 1.5 μm in Er^{3+}:Y_2SiO_5 versus magnetic field, temperature, and Er^{3+} concentration, Phys. Rev. B **73**, 075101 (2006).

[37] C. Thiel, R. M. Macfarlane, Y. Sun, T. Böttger, N. Sinclair, W. Tittel, and R. Cone, Measuring and analyzing excitation-induced decoherence in rare-earth-doped optical materials, Laser Phys. **24**, 106002 (2014).

[38] H. de Vries and D. A. Wiersma, Photophysical and photochemical molecular hole burning theory, J. Chem. Phys. **72**, 1851 (1980).

[39] Z. Bai, Z. Zhao, Y. Qi, J. Ding, S. Li, X. Yan, Y. Wang, and Z. Lu, Narrow-linewidth laser linewidth measurement technology, Front. Phys. **9**, 768165 (2021).

[40] R. G. Brewer and R. Shoemaker, Optical free induction decay, Phys. Rev. A **6**, 2001 (1972).

[41] Y. S. Bai and R. Kachru, Spin-fluctuation-induced optical spectral diffusion in Pr^{3+}:$YAlO_3$, Phys. Rev. A **44**, R6990(R) (1991).

[42] R. Yano, M. Mitsunaga, and N. Uesugi, Stimulated-photon-echo spectroscopy. I. Spectral diffusion in Eu^{3+}:$YAlO_3$, Phys. Rev. B **45**, 12752 (1992).

[43] J. H. Van Vleck, *The Theory of Electric and Magnetic Susceptibilities* (Clarendon Press, Oxford, 1932).

[44] Y. Takikawa, S. Ebisu, and S. Nagata, Van Vleck paramagnetism of the trivalent Eu ions, J. Phys. Chem. Solids **71**, 1592 (2010).

[45] A. Ortu, A. Tiranov, S. Welinski, F. Fröwis, N. Gisin, A. Ferrier, P. Goldner, and M. Afzelius, Simultaneous coherence enhancement of optical and microwave transitions in solid-state electronic spins, Nat. Mater. **17**, 671 (2018).

[46] G. Huang, H. Liu, H. Dong, and Z. He, Investigation of the clock transition and its pressure-dependent behavior of the trigonal $^{171}Yb^{3+}$ centers in lithium niobate crystal, J. Appl. Phys. **133**, 205103 (2023).

[47] R. Valivarthi, P. Umesh, C. John, K. A. Owen, V. B. Verma, S. W. Nam, D. Oblak, Q. Zhou, and W. Tittel, Measurement-device-independent quantum key distribution coexisting with classical communication, Quantum Sci. Technol. **4**, 045002 (2019).

[48] L. Li, A. B. Karyath, J. Bertrand, M. Falamarzi Askarani, M. Gieysztor, H. Meppully Sasidharan, J. A. Slater, A. D. Marsh, P. J. T. Woodburn, C. W. Thiel, R. L. Cone, S. Marzban, N. Alfasi, P. Remy, and W. Tittel, Experimental data for paper "Spectroscopy and coherence of an excited-state transition in Tm3+:YAlO3 at telecommunication wavelength", Zenodo, 2026, https://doi.org/10.5281/zenodo.20024931.

[49] G. Asatryan and J. Rosa, EPR of Er^{3+}, Nd^{3+}, and Ce^{3+} ions in $YAlO_3$ single crystals, Phys. Solid State **44**, 864 (2002).

[50] F. Wang, M. Ren, W. Sun, M. Guo, M. J. Sellars, R. L. Ahlefeldt, J. G. Bartholomew, J. Yao, S. Liu, and M. Zhong, Nuclear spins in a solid exceeding 10-hour coherence times for ultra-long-term quantum storage, PRX Quantum **6**, 010302 (2025).

[51] G. Heinze, C. Hubrich, and T. Halfmann, Coherence time extension in Pr^{3+}:Y_2SiO_5 by self-optimized magnetic fields and dynamical decoupling, Phys. Rev. A **89**, 053825 (2014).

[52] M. Rančić, M. P. Hedges, R. L. Ahlefeldt, and M. J. Sellars, Coherence time of over a second in a telecom-compatible quantum memory storage material, Nat. Phys. **14**, 50 (2018).

[53] J. M. Kindem, J. G. Bartholomew, P. J. T. Woodburn, T. Zhong, I. Craiciu, R. L. Cone, C. W. Thiel, and A. Faraon, Characterization of $^{171}Yb^{3+}$:YVO_4 for photonic quantum technologies, Phys. Rev. B **98**, 024404 (2018).

[54] J. V. Rakonjac, Y.-H. Chen, S. P. Horvath, and J. J. Longdell, Long spin coherence times in the ground state and in an optically excited state of $^{167}Er^{3+}$:Y_2SiO_5 at zero magnetic field, Phys. Rev. B **101**, 184430 (2020).

[55] S. Welinski, P. J. T. Woodburn, N. Lauk, R. L. Cone, C. Simon, P. Goldner, and C. W. Thiel, Electron spin coherence in

optically excited states of rare-earth ions for microwave to optical quantum transducers, Phys. Rev. Lett. **122**, 247401 (2019).

[56] C. W. Thiel, N. Sinclair, W. Tittel, and R. L. Cone, Optical decoherence studies of Tm^{3+}:$Y_3Ga_5O_{12}$, Phys. Rev. B **90**, 214301 (2014).

[57] R. W. Equall, R. L. Cone, and R. M. Macfarlane, Homogeneous broadening and hyperfine structure of optical transitions in Pr^{3+}:Y_2SiO_5, Phys. Rev. B **52**, 3963 (1995).

[58] S. Wang, L. Yang, M. Shen, W. Fu, Y. Xu, R. L. Cone, C. W. Thiel, and H. X. Tang, Er^{3+}:$LiNbO_3$ with high optical coherence enabling optical thickness control, Phys. Rev. Appl. **18**, 014069 (2022).

[59] A. Zangwill, *Modern Electrodynamics* (Cambridge University Press, Cambridge, UK, 2013).

[60] P. W. Milonni and J. H. Eberly, *Laser Physics* (John Wiley & Sons, Hoboken, New Jersey, 2010).

[61] R. W. Boyd, *Nonlinear Optics* (Academic Press, Cambridge, Massachusets, 2020).

[62] T. Böttger, C. W. Thiel, R. L. Cone, Y. Sun, and A. Faraon, Optical spectroscopy and decoherence studies of Yb^{3+}:YAG at 968 nm, Phys. Rev. B **94**, 045134 (2016).

[63] S. K. Seth, J. Nagura, V. Somjit, A. Bapat, X. Li, G. D. Grant, I. Masiulionis, X. Han, F. J. Heremans, G. Galli, *et al.*, Spin decoherence dynamics of Er^{3+} in CeO_2 films, Phys. Rev. Lett. **135**, 266901 (2025).

[64] M. Afzelius, C. Simon, H. de Riedmatten, and N. Gisin, Multimode quantum memory based on atomic frequency combs, Phys. Rev. A **79**, 052329 (2009).

[65] M. Afzelius and C. Simon, Impedance-matched cavity quantum memory, Phys. Rev. A **82**, 022310 (2010).

[66] J. H. Davidson, P. Lefebvre, J. Zhang, D. Oblak, and W. Tittel, Improved light-matter interaction for storage of quantum states of light in a thulium-doped crystal cavity, Phys. Rev. A **101**, 042333 (2020).

[67] R.-R. Meng, P.-X. Liu, X. Liu, T.-X. Zhu, P.-J. Liang, C. Zhang, Z.-Y. Tang, H.-Z. Zhang, J.-M. Cui, M. Jin, *et al.*, Efficient integrated quantum memory for light, Nat. Photonics **20**, 437 (2026).

[68] P. Seidler, K. Lister, U. Drechsler, J. Hofrichter, and T. Stöferle, Slotted photonic crystal nanobeam cavity with an ultrahigh quality factor-to-mode volume ratio, Opt. Express **21**, 32468 (2013).